Title

Regularization design in penalized maximum-likelihood image reconstruction for lesion detection in 3D PET

Journal

Physics in Medicine and Biology, 59(2)

ISSN

0031-9155

Authors

Yang, Li
Zhou, Jian
Ferrero, Andrea
et al.

Publication Date

2014-01-20

DOI

10.1088/0031-9155/59/2/403

Peer reviewed

Published in final edited form as:
Phys Med Biol. 2014 January 20; 59(2): 403–419. doi:10.1088/0031-9155/59/2/403.

Regularization design in penalized maximum-likelihood image reconstruction for lesion detection in 3D PET

Li Yang, **Jian Zhou**, **Andrea Ferrero**, **Ramsey D. Badawi**, and **Jinyi Qi**
Department of Biomedical Engineering, University of California, Davis, CA, USA

Department of Radiology, UC Davis Medical Center, Sacramento, CA, USA

Jinyi Qi: qi@ucdavis.edu

Abstract

Detecting cancerous lesions is a major clinical application in emission tomography. In previous work, we have studied penalized maximum-likelihood (PML) image reconstruction for the detection task and proposed a method to design a shift-invariant quadratic penalty function to maximize detectability of a lesion at a known location in a two dimensional (2D) image. Here we extend the regularization design to maximize detectability of lesions at unknown locations in fully 3D PET. We used a multiview channelized Hotelling observer (mvCHO) to assess the lesion detectability in 3D images to mimic the condition where a human observer examines three orthogonal views of a 3D image for lesion detection. We derived simplified theoretical expressions that allow fast prediction of the detectability of a 3D lesion. The theoretical results were used to design the regularization in PML reconstruction to improve lesion detectability. We conducted computer-based Monte Carlo simulations to compare the optimized penalty with the conventional penalty for detecting lesions of various sizes. Only true coincidence events were simulated. Lesion detectability was also assessed by two human observers, whose performances agree well with that of the mvCHO. Both the numerical observer and human observer results showed a statistically significant improvement in lesion detection by using the proposed penalty function compared to using the conventional penalty function.

1. Introduction

Statistical reconstruction methods based on the penalized maximum-likelihood (PML) principle have been developed to improve image quality, e.g., Fessler (1994), Mumcuoglu *et al* (1994), Fessler and Hero (1995), Bouman and Sauer (1996). A number of metrics have been used to evaluate the quality of the reconstructed PET images, such as spatial resolution, noise variance, contrast-to-noise ratio, etc. Work has been done to designed quadratic penalty functions to achieve uniform resolution (Stayman and Fessler 2000, Qi and Leahy 2000, Shi and Fessler 2009) and to maximize the contrast-to-noise ratio (Qi and Leahy 1999). However, these technical metrics do not necessarily reflect the performance of a clinical task.

Here we focus on the task of lesion detection and use a task-specific metric to evaluate the image quality. A standard methodology to evaluate lesion detectability is the receiver operating characteristic (ROC) curve that compares the true-positive rate versus false-positive rate for human observers. The area under the ROC curve (AUC) is often used as a measure of the detection performance. Since human observers can be time-consuming, numerical observers based on the signal-detection theory have been developed to evaluate the lesion detectability (Barrett *et al* 1993). One popular numerical observer for lesion detection in a 2D image is the Channelized Hotelling observer (CHO) (Yao and Barrett 1992, Myers and Barrett 1987) which have been shown to have good correlation with human performance. The performance of a CHO can be measured by the signal-to-noise ratio (SNR) of the test statistic of the observer. Based on the theoretical analysis of the spatial resolution and noise properties of quadratically regularized image reconstruction (Fessler 1996, Fessler and Rogers 1996, Qi and Leahy 1999, 2000, Bonetto *et al* 2000), Qi (2004) derived simplified theoretical expressions that allow fast evaluation of the lesion detectability. Qi and Huesman (2006) applied the theoretical results to guide the design of a spatially invariant quadratic penalty function to maximize the lesion detectability at a fixed lesion location, i.e., a signal known exactly and background known exactly (SKE/BKE) task.

Recently we have extended the method in (Qi and Huesman 2006) to the design of a shift-variant penalty function for detection of a lesion at an unknown location. A common approach to include location uncertainty in lesion detection is through the use of a localization ROC (LROC) curve, which plots the fraction of correctly localized positive lesions vs. the false negative rate (Swensson 1996, Gifford *et al* 2003, Khurd *et al* 2003). The area under the LROC curve, A_{LROC}, can then be calculated to measure the lesion detection and localization performance. However, finding a shift-variant penalty function that maximizes A_{LROC} directly is impractical because of the huge number of parameters involved in the optimization. Given the relationship between the ROC curve and LROC curve (Swensson 1996, Gifford *et al* 1999), we instead focus on designing a penalty function that maximizes the ROC performance at all possible locations. For every voxel, we can predict the detectability of a lesion at that voxel using the simplified theoretical expressions, and then find the optimum local weighting parameters of a quadratic penalty function to maximize the lesion detectability. The optimum local weighting parameters at different locations are combined to form a spatially variant penalty function for image reconstruction. Preliminary results in a two dimensional case have been presented at a conference (Yang *et al* 2012). This paper further extends the quadratic regularization design from two dimensional (2D) to fully 3D PET. The proposed penalty design is patient-specific because it takes into account the tracer distribution and noise statistics estimated from the patient emission data. While there is also a large body of literature developing edge-preserving priors, so far quantitative evaluations have not found significant improvement in lesion detection performance by using edge-preserving penalty functions (Qi 2005, Nuyts *et al* 2009). Therefore, we focus on the design of a quadratic penalty function.

Beside the differences in image reconstruction, 3D regularization design differs from the 2D case in the numerical observer model that is used to measure the detection performance.

Several numerical observer models have been proposed for lesion detection in 3D images. Liang *et al* (2008) used the conventional 2D CHO and applied it to a single image slice where the signal is centered. Kim *et al* (2004) proposed a 3D CHO model that applied 3D frequency selective channel functions directly to a 3D image. Platiša *et al* (2011) compared the two CHO models mentioned above with the multislice CHO (msCHO), but with an objective to find the most efficient CHO. The msCHO applies a conventional 2D frequency selective channels to several consecutive slices that contain the target, and then combine these slice assessments to compute the final test statistic. Based on the observation that a human observer often examine not only neighboring slice but also orthogonal views around a suspected lesion location, Chen *et al* (2002) and Gifford *et al* (2006) applied 2D channels to multiple slices in each of the three orthogonal views (transaxial, coronal and sagittal), then combined the channel outputs into a test statistic by a Hotelling observer. We refer to this model as the multislice multiview CHO. Since we focus on small lesion detection task here and to save computation cost, we applied a single slice CHO on each three orthogonal views to measure the lesion detectability. We referred to this observer model as the multiview CHO (mvCHO). In our experiments, we observed that the multiview CHO could provide a higher SNR for lesion detection than either the single slice CHO or the multislice CHO, and approaches the performance of the multislice multiview CHO for small lesion case.

This paper is organized as follows. In Section 2 we first present the theory of PML image reconstruction and lesion detection. Then we describe how to design a quadratic penalty function for lesion detection. In Section 3 we describe the methods for the evaluation study. The Monte Carlo simulation results and human observer study results are given in Section 4. A discussion is included in Section 5. Finally we draw conclusions in Section 6.

2. Theory

2.1. Penalized maximum-likelihood image reconstruction

In emission tomography, the measured sinogram data, $\boldsymbol{y} \in \mathscr{R}^{M \times 1}$, can be modeled as a collection of independent Poisson random variables with the expectation, $\bar{\boldsymbol{y}} \in \mathscr{R}^{M \times 1}$, related to the unknown tracer distribution, $\boldsymbol{x} \in \mathscr{R}^{N \times 1}$, through an affine transformation

$$\bar{\boldsymbol{y}} \equiv E[\boldsymbol{y}|\boldsymbol{x}] = \boldsymbol{P}\boldsymbol{x} + \boldsymbol{r}, \quad (1)$$

where $E[\cdot|\cdot]$ denotes conditional expectation, $\boldsymbol{P} \in \mathscr{R}^{M \times N}$ is the detection probability matrix with the (i, j)th element equal to the probability of detecting an event from the jth voxel at the ith projection element, and $\boldsymbol{r} \in \mathscr{R}^{M \times 1}$ is the expectation of the background events (scattered and random events) in the data. The log likelihood function is given by

$$L(\boldsymbol{y}|\boldsymbol{x}) = \sum_i (y_i \log \bar{\boldsymbol{y}}_i - \bar{\boldsymbol{y}}_i - \log y_i!). \quad (2)$$

Penalized likelihood methods regularize the image reconstruction through the use of a roughness penalty function. Here we focus on quadratic penalty functions because quantitative studies have not found that edge-preserving penalty functions provide

improvement to lesion detection task (Qi 2005, Nuyts *et al* 2009). The quadratic penalty function is expressed as

$$\phi(\boldsymbol{x})=\frac{1}{2}\boldsymbol{x}'\boldsymbol{R}\boldsymbol{x}, \quad (3)$$

where $\boldsymbol{R}$ is a positive semi-definite matrix and '′' denotes vector (or matrix) transpose. Combining the likelihood function and the penalty function, the PML solution is found by

$$\hat{\boldsymbol{x}}(\boldsymbol{y})=\underset{\boldsymbol{x}\geq 0}{\operatorname{argmax}}[L(\boldsymbol{y}|\boldsymbol{x})-\beta\phi(\boldsymbol{x})], \quad (4)$$

where β is a parameter that controls the degree of regularization.

2.2. Lesion detection with numerical observer

For a given reconstructed image $\boldsymbol{x}$, a numerical observer computes a scalar test statistic $\eta(\boldsymbol{x})$ and compares it with a threshold to determine whether the image is normal or abnormal. The test statistic of the 2D CHO is computed by

$$\eta_{\mathrm{CHO}}(\hat{\boldsymbol{x}})=\boldsymbol{z}'\boldsymbol{U}'\boldsymbol{K}^{-1}(\boldsymbol{U}\hat{\boldsymbol{x}}+\boldsymbol{n}), \quad (5)$$

where $\boldsymbol{z}$ is the expected profile of the reconstructed lesion, i.e., $\boldsymbol{z} = E[\boldsymbol{x}|H_1]-E[\boldsymbol{x}|H_0]$ (H_0 is the null hypothesis representing lesion absent and H_1 is the alternative hypothesis representing lesion present), $\boldsymbol{U}$ denotes a set of frequency-selective channels that mimic the human visual system, $\boldsymbol{n}$ is the internal channel noise that models the uncertainty in human detection process with mean zero and covariance $\boldsymbol{K}_N$ (Yao and Barrett 1992). $\boldsymbol{K}$ is the covariance of the channel outputs and can be computed by

$$\boldsymbol{K}=\frac{1}{2}\boldsymbol{U}(\boldsymbol{\Sigma}_{\hat{\boldsymbol{x}}|H_1}+\boldsymbol{\Sigma}_{\hat{\boldsymbol{x}}|H_0})\boldsymbol{U}'+\boldsymbol{K}_N, \quad (6)$$

where $\boldsymbol{\Sigma}_{\boldsymbol{x}|H_1}$ and $\boldsymbol{\Sigma}_{\boldsymbol{x}|H_0}$ are the covariance matrices of $\boldsymbol{x}$ under hypotheses of H_1 and H_0, respectively.

The detection performance can be measured by the SNR of $\eta(\boldsymbol{x})$, which is defined as

$$\mathrm{SNR}^2[\eta(\hat{\boldsymbol{x}})]=\frac{(E[\eta(\hat{\boldsymbol{x}})|H_1]-E[\eta(\hat{\boldsymbol{x}})|H_0])^2}{(\mathrm{var}[\eta(\hat{\boldsymbol{x}})|H_1]+\mathrm{var}[\eta(\hat{\boldsymbol{x}})|H_0])/2}. \quad (7)$$

When $\eta(\boldsymbol{x})$ is normally distributed, AUC is related to SNR by

$$\mathrm{AUC}=\frac{1}{2}\left[1+\mathrm{erf}\left(\frac{\mathrm{SNR}}{2}\right)\right] \quad (8)$$

where erf(·) is the error function.

For lesion detection in 3D images, we use a multiview channelized Hotelling observer (mvCHO) to assess lesion detectability to mimic the condition where a human observer examines three orthogonal views to detect a lesion. The mvCHO applies 2D frequency

selective channels to each of the three orthogonal (transaxial, coronal and sagittal) views of a 3D image and combines the channel outputs into a test statistic using a Hotelling observer. The test statistic of the mvCHO can be computed by

$$\eta_{\mathrm{mvCHO}}(\hat{\boldsymbol{x}})=\boldsymbol{z}'\boldsymbol{U}'\boldsymbol{K}^{-1}(\boldsymbol{U}\hat{\boldsymbol{x}}+\boldsymbol{n}), \quad (9)$$

which has the same form as equation (5), but with $\boldsymbol{U}$ being the collection of 2D frequency selective channels in three orthogonal views. Substituting (9) into (7), we can compute the SNR of the multiview CHO by

$$\mathrm{SNR}^2_{\mathrm{mvCHO}}(\hat{\boldsymbol{x}})=\boldsymbol{z}'\boldsymbol{U}'\boldsymbol{K}^{-1}\boldsymbol{U}\boldsymbol{z}. \quad (10)$$

2.3. Fast computation of lesion detectability

To compute the SNR of the multiview CHO, we need expressions for $\boldsymbol{z} = E[\boldsymbol{x}|\hat{H}_1] - E[\boldsymbol{x}|\hat{H}_0]$ and covariance matrices $\boldsymbol{\Sigma}_{\boldsymbol{x}|\hat{H}_1}$ and $\boldsymbol{\Sigma}_{\boldsymbol{x}|\hat{H}_0}$. The spatial resolution and noise properties of quadratically regularized image reconstructions has been well studied and can be estimated analytically. Using theoretical results given by Qi (2004), $\boldsymbol{z}$ and the covariance matrices can be approximated by

$$\boldsymbol{z} \approx [\boldsymbol{F}+\beta\boldsymbol{R}]^{-1}\boldsymbol{F}\bar{\boldsymbol{f}}_l \quad (11)$$

$$\boldsymbol{\Sigma}_{\hat{\boldsymbol{x}}|H_k} \approx [\boldsymbol{F}+\beta\boldsymbol{R}]^{-1}\boldsymbol{F}[\boldsymbol{F}+\beta\boldsymbol{R}]^{-1}, k=0,1, \quad (12)$$

where $\boldsymbol{F}=\boldsymbol{P}'\mathrm{diag}[\frac{1}{\bar{\boldsymbol{y}}}]\boldsymbol{P}$ is the Fisher information matrix, $\bar{\boldsymbol{f}}_l \equiv E[\boldsymbol{x}|H_1] - E[\boldsymbol{x}|H_0]$ is the expectation of the lesion profile. Here we assumed the covariance to be the same for H_0 and H_1, since the presence of a small lesion has little effect on the variance of PET data. Details on the derivation of $\boldsymbol{z}$ and $\boldsymbol{\Sigma}_{\boldsymbol{x}|\hat{H}_k}$ can be found in (Qi 2004).

Substituting (11) and (12) into (10), we can obtain the theoretical expressions of the SNR of the multiview CHO as

$$\mathrm{SNR}^2_{\mathrm{mvCHO}} \approx \bar{\boldsymbol{f}}_l'\boldsymbol{F}[\boldsymbol{F}+\beta\boldsymbol{R}]^{-1}\boldsymbol{U}'\boldsymbol{K}^{-1}\boldsymbol{U}[\boldsymbol{F}+\beta\boldsymbol{R}]^{-1}\boldsymbol{F}\bar{\boldsymbol{f}}_l \quad (13)$$

where

$$\boldsymbol{K} \approx \boldsymbol{U}[\boldsymbol{F}+\beta\boldsymbol{R}]^{-1}\boldsymbol{F}[\boldsymbol{F}+\beta\boldsymbol{R}]^{-1}\boldsymbol{U}'+\boldsymbol{K}_N. \quad (14)$$

For fast computation, we approximate $\boldsymbol{F}$ and $\boldsymbol{R}$ locally using circulant matrices $\hat{\boldsymbol{F}}$ and $\hat{\boldsymbol{R}}$, respectively, based on the observation that $\boldsymbol{F}$ and $\boldsymbol{R}$ vary smoothly in space and $\bar{\boldsymbol{f}}_l$ and $\boldsymbol{U}$ have relatively compact support (Qi and Leahy 2000, Stayman and Fessler 2000). Matrices $\hat{\boldsymbol{F}}$ and $\hat{\boldsymbol{R}}$ are constructed using the column vectors of $\boldsymbol{F}$ and $\boldsymbol{R}$ corresponding to the voxel at the center of lesion, respectively. Because circulant matrices can be diagonalized by the Fourier transform, we can evaluate (13) quickly using the fast Fourier transform as

$$\mathrm{SNR}^2_{\mathrm{mvCHO}} \approx \left[\sum_i \frac{\tilde{U}_{k,i}\lambda_i\xi_i}{\lambda_i+\beta\mu_i}\right]' \boldsymbol{K}^{-1} \left[\sum_i \frac{\tilde{U}_{k,i}\lambda_i\xi_i}{\lambda_i+\beta\mu_i}\right] \quad (15)$$

where

$$\boldsymbol{K} \approx \tilde{\boldsymbol{U}}\,\mathrm{diag}\left[\frac{\lambda_i}{(\lambda_i+\beta\mu_i)^2}\right]\tilde{\boldsymbol{U}}' + \boldsymbol{K}_N. \quad (16)$$

Here $\tilde{\boldsymbol{U}}$ are the Fourier coefficients of the channel functions, $\{\xi_i\}_{i=1}^N$ is the Fourier transform of $\bar{\boldsymbol{f}}$, and $\{\lambda_i\}_{i=1}^N$ and $\{\mu_i\}_{i=1}^N$ are the eigenvalues (Fourier coefficients) of $\hat{\boldsymbol{F}}$ and $\hat{\boldsymbol{R}}$, respectively.

2.4. Regularization design for lesion detection

For a given dataset, equation (15) can be used to evaluate lesion detectability under different regularization parameters and to guide penalty design. The calculation of the Fisher information matrix requires the mean of the data, which can be estimated by either a forward projection of an initial reconstruction or a data plug-in method (Fessler and Rogers 1996, Qi and Leahy 2000). We used the modified data plug-in method proposed in (Qi and Leahy 2000) that approximates $1/\bar{y}$ by $1/(y + 1)$. It guarantees a positive denominator for any Poisson random variable y and eliminates the need to identify sinogram bins with zero mean in the calculation. The method works well for noisy data with an average count per sinogram bin greater than 3 (see Figure 16 in (Qi and Leahy 2000)). For data with lower counts, a more sophisticated method that has been proposed by Li *et al* (2004) can be used. Therefore, for a given set of patient data, we can estimate the Fisher information matrix and then find the proper values of $\{\beta\mu_i\}_{i=1}^N$ (and hence $\boldsymbol{R}$) by maximizing the SNR of mvCHO given in equation (15).

Without loss of generality, we can set β to a fixed value and maximize SNR by varying $\{\mu_i\}_{i=1}^N$. To reduce the number of unknowns, we decompose the quadratic penalty function into pairwise penalties in the following form

$$\boldsymbol{x}'\boldsymbol{R}\boldsymbol{x} = \sum_{j=1}^{N}\sum_{l\in\mathcal{N}_j}\gamma_{jl}(x_j - x_l)^2 \quad (17)$$

where $\mathcal{N}_j$ denotes the neighborhood of the jth pixel and γ_{jl} is the weighting factor for the pairwise penalty. For the conventional first-order quadratic penalty, the neighborhood $\mathcal{N}_j$ contains the 4 nearest neighboring pixels in 2D (6 nearest neighboring voxels in 3D) and all the weighting factor γ_{jl} equal to one. Using equation (17), we can express μ_i as a function of γ_{jl}:

$$\mu_i^j = \sum_l \gamma_{jl}\mu_i^l, \quad (18)$$

where μ_i^l is the frequency response of the *l*th pairwise penalty. Note that μ_i in equation (15) becomes μ_i^j and can vary from voxel to voxel, and $\mathrm{SNR}^2_{\mathrm{mvCHO}}$ in equation (15) becomes a function of γ_{jl}. Therefore, we can estimate the weighting factors γ_{jl} to maximize the lesion detectability at voxel *j* and repeat this procedure for all voxels. The final penalty function is computed as

$$\boldsymbol{x}'\boldsymbol{R}\boldsymbol{x}=\sum_{j=1}^{N}\sum_{l\in\mathcal{N}_j}\frac{\gamma_{jl}+\gamma_{lj}}{2}(x_j-x_l)^2 \quad (19)$$

to ensure that $\boldsymbol{R}$ is symmetric. Note that the optimum γ_{jl} are independent of the count level of the data and the contrast of the lesion (Qi 2004).

One constraint on the weighting factors is that the resulting $\boldsymbol{R}$ should be positive semi-definite, which can be satisfied by constraining all γ_{jl} to be nonnegative. Although $\gamma_{jl} \geq 0$ is a sufficient, but not necessary, condition, we found little improvement in CHO SNR by allowing γ_{jl} to take negative values in our experiments. The penalty design thus reduces to compute the optimal weighting factors at each pixel *j* by

$$\{\gamma_{jl}\}=\underset{\gamma_{jl}\geq 0}{\operatorname{argmax}}\,\mathrm{SNR}^2_{\mathrm{mvCHO}}. \quad (20)$$

Performing the optimization in (20) for every pixel can be time-consuming. To reduce the computation cost, we only compute the optimum weighting factors on a coarse grid and then assign the values of γ_{jl} to other pixels using the nearest neighbor interpolation (Yang *et al* 2012). We found that γ_{jl} varies slowly as we move from one pixel to its neighbors, so the interpolation works well. A pseudocode outlining the procedure is given in Algorithm table 1.

Algorithm 1

Procedure to design the penalty function for lesion detection

1: For a given sinogram $\boldsymbol{y}$, approximate $\mathrm{diag}[\frac{1}{\bar{\boldsymbol{y}}}]$ by $\mathrm{diag}[\frac{1}{\boldsymbol{y}+1}]$ (Qi and Leahy 2000).‡.

2: Precompute the Fourier coefficients of the channel functions, $\boldsymbol{\theta}$.

3: Precompute μ_i^l, which is the frequency response of the pairwise penalties for the neighborhood $\mathcal{N}_j$.

4: **for** each voxel *j* on the coarse grid **do**

5: A small lesion $\boldsymbol{f_l}$ is simulated as a hot spot at voxel *j*, and compute its Fourier transform $\{\xi_i\}_{i=1}^N$.

6: Forward project the *j*th unit vector e_j by the system matrix $\boldsymbol{P}$ to obtain $\boldsymbol{P}e_j$.

7: Perform a weighted back projection to get $\boldsymbol{P}'\mathrm{diag}[\frac{1}{\boldsymbol{y}+1}]\boldsymbol{P}e_j$, which is the column vector of $\boldsymbol{F}$ corresponding to the voxel at the center of lesion.

‡For low-count data, the method in (Li *et al* 2004) should be used.

8: Compute the Fourier coefficients of $\boldsymbol{P}'\mathrm{diag}[\frac{1}{\boldsymbol{y}+1}]\boldsymbol{P}e_j$ to obtain $\{\lambda_i\}_{i=1}^{N}$.

9: Use Matlab function "fmincon" to estimate the weighting factors γ_{jl} that maximize $\mathrm{SNR}^2_{\mathrm{mvCHO}}$ in equation (15) while keeping β at a fixed value.

10: **end for**

11: **for** each voxel *k* not on the coarse grid **do**

12: Assign the weighting factors based on its nearest neighbor in the coarse grid.

13: **end for**

14: Form the proposed penalty function using equation (19) and perform penalized maximum-likelihood image reconstruction.

3. Simulation Methods

3.1. PET Scanner and the digital phantom

The proposed method can be applied to detection of small lesions and metastases of various cancers. Here we focus our simulation study to breast cancer. The reason is two-fold. The first one is that breast cancer is the most frequently diagnosed cancer in women. PET imaging has played a significant and evolving role in the staging, followup and management of metastatic breast cancer. However, current FDG-PET has low sensitivity to detect micrometastases and small tumor-infiltrated lymph nodes (Avril and Adler 2007). Here we intend to improve the detection performance of small breast tumors by developing a sophisticated image reconstruction method. The second reason is that the malignancy of a breast lesion can be verified by histological examination for patients undergoing breast surgery. The ability to obtain the ground truth is critical for future validation of the proposed method in patient studies, although we only focus on computer simulation studies here.

The simulated 3D PET system has same parameters as a GE DST clinical scanner (Guérin and Fakhri 2008). The digital phantom was created from a patient PET/CT scan as shown in Figure 1, where there was a histologically verified tumor in the left breast. Currently PET imaging of breast cancer is often used to detect distant metastases for staging purpose. Thus we simulated detection of a small tumor in the contralateral breast and other soft tissue. We segmented the implant, the fat and glandular tissue in the contralateral breast and assigned a uniform activity to each tissue type based on the original PET image. The corresponding CT scan was used to compute the attenuation correction factors. There is some truncation in the original CT image, so we estimated the truncated region in the CT image using the coregistered PET image and assign it to soft tissue.

A small lesion was simulated as a hot spot of 3 mm in diameter with contrast 2.2 to 1, as shown in Figure 2(a). To evaluate the proposed penalty design method for detecting a tumor at an unknown position, we inserted this small lesion at five different locations in two slices. To investigate whether the proposed penalty function optimized for small lesion detection would reduce the detectability of a larger lesion, we also simulated a larger lesion with a diameter of 8 mm as shown in Figure 2(b). For each lesion location, the phantom images with and without a lesion were forward projected to generate noise-free projections, using a

solid-angle based analytically calculated system matrix (Qi *et al* 1998). Independent Poisson noise was then added to the noise-free sinogram to generate 200 independent realizations with the expected total number of events equal to one hundred million. We did not include the scatters and randoms in the computer simulation in this study. The impact of this limitation will be discussed in Section 5.

3.2. Image reconstruction

The noisy data were reconstructed using two penalty functions: (1) the first-order quadratic penalty function and (2) the proposed penalty function. We used the theoretical expression of the mvCHO SNR to find the optimal penalty function which achieves the highest SNR for the lesion detection. We first computed the optimal weighting factor γ_{jl} based on equation (20) for 72 selected locations in three slices (represented by the "+" marks in Figure 3). We chose a large $\mathcal{N}_j$ that included 92 nearest voxels. Because of the symmetry, only 46 independent γ_{jl} need to be determined at each preselected location. Here we fixed β value at 10^{-6} (which is in the same range of β used for the first-order quadratic penalty for easy comparison) when estimating the weighting factor γ_{jl}. The weights at other voxels were assigned based on its nearest neighbor in the 72 samples. The proposed penalty matrix $\boldsymbol{R}$ was then formed by equation (19). We reconstructed the 200 pairs of noisy data sets using he proposed penalty function and the conventional first-order quadratic penalty function with different β values. All images were reconstructed using 180 × 180 × 49 cubic voxels of 3.27 × 3.27 × 3.27 mm^3.

3.3. Numerical observer

The multiview CHO was used to measure the lesion detectability. The channel functions of the multiview CHO were three difference-of-Gaussian (DOG) channels as used in Abbey and Barrett (1996). There have been several models of internal noise proposed in the literature. The simplest form as used in Abbey and Barrett (2001) is Gaussian noise with zero mean and covariance $\boldsymbol{K}_N = \alpha_1 \boldsymbol{I}$, where $\boldsymbol{I}$ is the identity matrix and α_1 is a scaling factor. Oldan *et al* (2004) modeled the internal noise as Gaussian noise with zero mean and covariance $\boldsymbol{K}_N = \mathrm{diag}[\alpha_2\sigma_i^2 + \alpha_3 \max_i\{\sigma_i^2\}]$, where σ_i^2 is the data variance in the *i*th channel output, α_2 and α_3 are two scaling factors which can be found by minimizing the difference between the numerical observer results and human observer results. The internal noise we used in this paper is the combination of the two models mentioned above. It is Gaussian noise with zero mean and covariance

$$\boldsymbol{K}_N = \alpha_1 \boldsymbol{I} + \mathrm{diag}[\alpha_2\sigma_i^2 + \alpha_3 \max_i\{\sigma_i^2\}]. \quad (21)$$

To find the parameters α_1, α_2 and α_3, we first reconstructed noisy data sets using the first-order quadratic penalty function with five different β values. A human observer study was performed to compare the theoretical prediction of lesion detectability with the human performance. The parameters were found by minimizing the mean square error between the SNRs of multiview CHO from the theoretical prediction and the human observer study.

3.4. Human observer study

A human observer study was performed to verify the numerical observer results. Two human observers (AF and LY) performed two-alternative force-choice (2AFC) experiments. They are both graduate student researchers in PET imaging at UC Davis. At each time a pair of reconstructed images, one with a tumor and one without, is presented to a human observer and the observer is asked to select the one with a tumor. For each lesion location, each observer read 200 images reconstructed using different penalty functions. The 200 reconstructed images were divided into two groups each with 100 samples. We used the first 10 image pairs in each group for training, where the observer received feedback on whether his choice was correct or not, and the remaining 90 image pairs for testing. For the first-order quadratic penalty function, we evaluated the images reconstructed with five different β values covering a wide range of regularization strength. For the proposed penalty, the two human observers read only the images reconstructed using the beta value that was optimized for lesion detection. In total each observer read 5 (lesion locations) × 6 (penalty functions) × 2 groups of reconstructed images, where the order of groups was randomly mixed. The resulting percent correct (PC) in the 2AFC test was converted to the SNR by (Burgess 1995)

$$\mathrm{SNR}=2\mathrm{erf}^{-1}(2\mathrm{PC}-1). \quad (22)$$

3.5. Statistical test

We performed a McNemar's test on the human observer 2AFC results to test the statistical significance of the difference. For each human observer, we compared the results using the proposed penalty function with those of the first-order quadratic penalty function. Each 2AFC experiment was considered as a Bernoulli experiment with two possible outcomes (0 for incorrect choice and 1 for correct choice). The outcomes of a pair of 2AFC experiments were sorted into four categories as shown in Table 1. From the observed value of N_1 to N_4, we computed the *p*-value under the McNemar's test.

4. Results

4.1. Internal noise parameters of the multiview CHO

The internal noise parameters found by minimizing the mean square error between the SNRs of multiview CHO from the theoretical prediction and the human observer study were $\alpha_1 = 1.58 \times 10^4$, $\alpha_2 = 0$ and $\alpha_3 = 0.144$. Figure 4 shows that the resulting internal noise model provided a more accurate prediction of the human observer performance than that without using the internal noise. Internal noise is critical for large β value to mimic the human performance because numerical observers can distinguish tiny differences between two reconstructed images, while a human cannot.

4.2. Comparison of different CHOs

We investigated the efficiencies of four CHOs for lesion detection. The first one is the single slice CHO, which applies a 2D CHO on the single transaxial slice through the center of a tumor. The second one is the multislice CHO, which applies 2D channels to three consecutive transaxial slices of the 3D image. The tumor is centered at the middle slice. The

third one is the multiview CHO, which applies 2D channels to three orthogonal slices through the center of the tumor. The last one is the multislice multiview CHO, which applies 2D channels to three consecutive slices in each three orthogonal views of the 3D image. All the four CHOs used the same 2D DOG channels and internal noise model in (21). To compare the lesion detectability quantitatively, we plotted the Monte Carlo SNR of the four CHOs for detecting a small and a large tumors in images reconstructed using the first-order quadratic penalty function with a series β values (Figure 5). Each Monte Carlo SNR was computed from 200 independently reconstructed image pairs.

The results show that the CHOs applied on three orthogonal views can extract additional information to distinguish the tumor than the single slice or multislice CHO that uses the transaxial view only, i.e. higher SNR for the multislice multiview CHO and multiview CHO than the single slice CHO and multislice CHO. For the smaller lesion, we observed similar performances between the multislice CHO and the single slice CHO because neighboring slices did not provide much information for detecting the lesion. The performances of the multislice multiview CHO and multiview CHO are also similar. Since we focus on small lesion detection task here, we chose the multiview CHO to assess lesion detectability in the 3D images and design the penalty function based on this model.

4.3. Lesion detectability using different penalty functions

Sample reconstructed images are shown in Figure 6. We compared the Monte Carlo SNR of the multiview CHO with the theoretical predictions at five locations as a function of β in Fig. 7 (left column). For the proposed penalty, we also included two additional β values, 10^{-5} and 10^{-7}, to show the lesion detectability with a stronger and weaker regularization. In general, the Monte Carlo results match the theoretical predictions very well. Both Monte Carlo and theoretical results show that the proposed penalty function improves lesion detectability over the conventional penalty by around 8%. Furthermore, we observed that the optimal β value of the first-order quadratic penalty function to achieve the maximum SNR varies for different lesion locations. It means multiple reconstructions with different β values would be necessary for detecting lesion at different locations when using the first-order quadratic penalty function, which would be impractical. In comparison, we only need to perform one reconstruction with the optimized penalty function to achieve the highest detection performance at all locations.

The results of two human observers are shown in Figure 7 middle and right columns. The human performances follow the same trends as those of the theoretical prediction. The resulting values of N_1 to N_4 for the McNemar's test are shown in Table 2. The *p*-values are given in the last row of Table 2. The results show that the proposed penalty function can significantly improve the lesion detection compared to the first-order quadratic penalty function in most cases.

4.4. Effect on detectability of larger lesions

To investigate whether the penalty function optimized for a 3 mm lesion would reduce the detectability of a larger lesion, we reconstructed the data that contained a 8 mm lesion using the penalty function optimized for the 3 mm lesion. Figure 8 plots the lesion detectability

estimated using the Monte Carlo method and the theoretical expression (15). The results show that although the penalty function was designed for the 3 mm lesion, it did not reduce the detectability of the 8 mm lesion.

5. Discussion

From the results shown in Table 2, we found that the number of cases benefited from using the proposed penalty is around 20 (= $N_4 - N_3$) on average for a total of 1000 cases. This is consistent with a ten percent improvement in SNR predicted by the theoretical expressions, which is equivalent to a two percent improvement in the percent correct of the 2AFC test. It is worthy noting that the improvement is over the optimum performance of the first-order penalty function, which is difficult to achieve in practice without an established method to select the optimum regularization parameter. Furthermore, the optimal β value of the first-order quadratic penalty function to achieve the maximum SNR varies for different lesion locations, which means multiple reconstruction with different β values may be necessary when using the first-order quadratic penalty function. In comparison, with the proposed optimized penalty function, we only need to perform one reconstruction with one set of regularization parameters to achieve the optimum detection performance at different locations.

5.1. Impact of scatters and random events

One limitation of the simulation study is that we did not model scatters and random events. However, we do not expect that inclusion of these background events would affect the design of the optimal penalty function because the penalty design depends only on the Fisher information matrix. To estimate the Fisher information matrix, we need to know the variance of the prompt data, but not a separate estimate of the background events. Because scatters and random events increase the number of counts of prompt data, they can improve the accuracy of the variance estimated by the data plug-in method (Qi and Leahy 2000). We note that imperfect scatter and random corrections can introduce additional variance in reconstructed images (Qi and Huesman 2002), but such corrections are unnecessary for lesion detection because these background events result in a common bias for both H_0 and H_1 hypotheses and doe not affect the lesion detectability for a well-trained observer. This is similar to the case where non-attenuation corrected PET images have been widely used before PET/CT was introduced.

5.2. Numerical observer for 3D images

From the results shown in Figure 7, we can see that the multiview CHO used in this paper can predict human performance very well. The Monte Carlo simulation results (Figure 5) show that the multiview CHO provides higher SNR for lesion detection than the single slice CHO and multislice CHO, and approaching the performance of the multislice multiview CHO for small lesion detection. Multislice CHO has a higher SNR than the single slice CHO for larger tumors, while their performances are similar for small tumors. These results are consistent with the findings by Platiša *et al* (2012) in their human observer study. Their results show an overall increase in human detection performance using multi-slice stack-browsing image presentation than viewing a single slice through the tumor center. In

addition, they found that the benefit from additional image slice in the multi-slice mode is larger for lower-complexity tasks, which corresponds to a large tumor detection task in our case. For 3D lesion detection, both the multiview CHO and multislice CHO can obtain more information for lesion detection than the single slice CHO does. We note that there is a lack of detailed comparison between the multiview CHO and multislice CHO, and more research is still needed to find an optimum anthropomorphic numerical observer for 3D lesion detection tasks.

5.3. Observer-specific numerical observer

Most existing numerical observers are not adapted to a particular human observer. However, human performance can still vary significantly from person to person. Even for a simple SKE/BKE detection task that used in this paper, two human observers results still differ. The last row in Figure 7 shows that the optimal β value using the first-order quadratic penalty function for LY is $10^{-6.7}$, while it is $10^{-6.3}$ for AF. As we are moving toward patient-adaptive PML reconstruction, it makes more sense to tailor the reconstruction for a specific observer. This requires estimating a numerical observer for each human observer. Estimation of the observer template for a given set of training data has been developed by Abbey and Eckstein (2002). However, for the purpose of designing the optimal penalty function, we need to predict the response of an observer to images that may have different resolution and noise characteristics from those in the training set. To solve this problem, it may be helpful to estimate observer-specific channel functions beyond the most commonly used non-overlapping square (SQR) channels or difference-of-Gaussian (DOG) channels. Estimation of channel functions and selecting the best channel parameters that correlates with a specific human observer will improve the accuracy in prediction of the human observer performance. An advantage of he proposed penalty design method is that it is independent of a particular choice of the numerical observer and can be applied to other numerical observers as well.

6. Conclusions

We have developed a method to design the quadratic penalty function in the penalized maximum-likelihood image reconstruction for 3D lesion detection. We used the multiview CHO to assess the lesion detectability, which showed good agreement with the human performance. Computer simulation results have shown that the proposed method can improve the lesion detectability over the conventional quadratic penalty function. We also demonstrated that using a penalty function designed for small lesions in reconstruction does not adversely affect the detection of larger lesions, which will allow us to focus on small lesion detectability in real patient data without worrying about the unknown lesion size. In future work, we will evaluate the proposed method using real patient data and also investigate the regularization for dynamic PET reconstruction.

Acknowledgments

This work was supported by the National Institutes of Health under grant no R01 EB 000194.

References

1. Abbey CK, Barrett HH. Observer signal-to-noise ratio for the ML-EM algorithm. Proc. SPIE. 1996; 3340:2–13.
2. Abbey CK, Barrett HH. Human- and model-observer performance in ramp-spectrum noise: effect of regularization an object variability. J. Opt. Soc. Am. A. 2001; 18:473–488.
3. Abbey CK, Eckstein MP. Optimal shifted estimates of human-observer templates in two-alternative forced-choice experiments. IEEE Trans. Med. Imaging. 2002; 21:429–440. [PubMed: 12071614]
4. Avril N, Adler LP. F-18 uorodeoxyglucose-positron emission tomography imaging for primary breast cancer and loco-regional staging Radiol. Clin. North Am. 2007; 45:645–657.
5. Barrett HH, Yao J, Rolland J, Myers K. Model observers for assessment of image quality. Proc. Natl. Acad. Sci. USA. 1993; 90:9758–9765. [PubMed: 8234311]
6. Bonetto P, Qi J, Leahy RM. Covariance approximation for fast and accurate computation of channelized Hotelling observer statistics. IEEE. Trans. Nucl. Sci. 2000; 47:1567–1572.
7. Bouman C, Sauer K. A unified approach to statistical tomography using coordinate decent optimization. IEEE Trans. Image Process. 1996; 5:480–492. [PubMed: 18285133]
8. Burgess AE. Comparison of receiver operating characteristic and forced choice observer performance measurement methods. Med. Phys. 1995; 22:643–655. [PubMed: 7643805]
9. Chen M, Bowsher J, Baydush A, Gilland K, Delong D, Jaszczak R. Using the hotelling observer on multislice and multiview simulated SPECT myocardial images. IEEE Trans. Nucl. Sci. 2002; 49:661–667.
10. Fessler JA. Penalized weighted least-squares image reconstruction for PET. IEEE Trans. Med. Imaging. 1994; 13:290–300. [PubMed: 18218505]
11. Fessler JA. Mean and variance of implicitly defined biased estimators (such as penalized maximum likelihood): applications to tomography. IEEE Trans. Image Process. 1996; 5:493–506. [PubMed: 18285134]
12. Fessler JA, Hero AO. Penalized maximum-likelihood image reconstruction using space-alternating generalized EM algorithms. IEEE Trans. Image Process. 1995; 4:1417–1429. [PubMed: 18291973]
13. Fessler JA, Rogers WL. Spatial resolution properties of penalized-likelihood image reconstruction: spatial-invariant tomographs. IEEE Trans. Image Process. 1996; 5:1346–1358. [PubMed: 18285223]
14. Gifford HC, Wells R, King MA. A comparison of human observer LROC and numerical observer ROC for tumor detection in SPECT images. IEEE Trans. Nucl. Sci. 1999; 46:1032–1037.
15. Gifford HC, Pretorius PH, King MA. Comparison of human- and model-observer LROC studies. Proc. SPIE. 2003; 5034:112–122.
16. Gifford, HC.; Lehovich, A.; King, MA. A multiclass model observer for multislice-multiview images; IEEE Nucl. Sci. Symp. Conf. Rec; 2006. p. 1687-1691.
17. Guérin B, Fakhri GE. Realistic PET Monte Carlo simulation with pixelated block detectors, light sharing, random coincidences and dead-time modeling. IEEE Trans. Nucl. Sci. 2008; 55:942–952. [PubMed: 19079776]
18. Khurd P, Gindi G. Rapid computation of LROC figures of merit using numerical observers (for SPECT/PET reconstruction). IEEE Trans. Nucl. Sci. 2003; 4:2516–2520. [PubMed: 20442799]
19. Kim JS, Kinahan P, Lartizien C, Comtat C, Lewellen T. A comparison of planar versus volumetric numerical observers for detection task performance in whole-body PET imaging. IEEE Trans. Nucl. Sci. 2004; 51:34–40.
20. Li Q, Asma E, Qi J, Bading JR, Leahy RM. Accurate estimation of the fisher information matrix for the PET image reconstruction problem. IEEE Trans. Med. Imaging. 2004; 23:1057–1064. [PubMed: 15377114]
21. Liang H, Park S, Gallas BD, Myers KJ, Badano A. Image browsing in slow medical liquid crystal displays. Acad. Radiol. 2008; 15:370–382. [PubMed: 18280935]

22. Mumcuoglu E, Leahy RM, Cherry S, Zhou Z. Fast gradient-based methods for Bayesian reconstruction of transmission and emission PET images. IEEE Trans. Med. Imaging. 1994; 13:687–701. [PubMed: 18218547]
23. Myers KJ, Barrett HH. Addition of a channel mechanism to the ideal-observer model. J. Opt. Soc. Am. A. 1987; 4:2447–2457. [PubMed: 3430229]
24. Nuyts J, Michel C, Brepoels L, Ceuninck LD, Deroose C, Goffin K, Mottaghy FM, Stroobants S, Riet JV, Verscuren R. Performance of MAP reconstruction for hot lesion detection in whole-body PET/CT: and evaluation with human and numerical observers. IEEE Trans. Med. Imaging. 2009; 28:67–73. [PubMed: 19116189]
25. Oldan J, Kulkarni S, Xing Y, Khurd P, Gindi G. Channelized Hotelling and human observer study of optimal smoothing in SPECT MAP reconstruction. IEEE Trans. Nucl. Sci. 2004; 51:733–741.
26. Platiša L, Goossens B, Vansteenkiste E, Park S, Gallas BD, Badano A, Philips W. Channelized Hotelling observers for the assessment of volumetric imaging data sets. J. Opt. Soc. Am. A. 2011; 28:1145–1163.
27. Platiša L, Kumcu A, Platišsa M, Vansteenkiste E, Deblaere K, Badano A, Philips W. Volumetric detection tasks with varying complexity: human observer performance. Proc. SPIE. 2012; 8318
28. Qi J. Analysis of lesion detectability in Bayesian emission reconstruction with non-stationary object variability. IEEE Trans. Med. Imaging. 2004; 23:321–329. [PubMed: 15027525]
29. Qi, J. Investigation of lesion detection and quantitation in MAP reconstruction with non-Gaussian priors; IEEE Nucl. Sci. Symp. Conf. Rec; 2005. p. 1704-1708.
30. Qi, j; Huesman, RH. Scatter Correction for Positron Emission Mammography. Phys. Med. Biol. 2002; 47:2759–2772. [PubMed: 12200937]
31. Qi J, Huesman RH. Penalized maximum-likelihood image reconstruction for lesion detection. Phys. Med. Biol. 2006; 51:4017–4029. [PubMed: 16885621]
32. Qi J, Leahy RM, Cherry SR, Chatziioannou A, Farquhar TH. High resolution 3D Bayesian image reconstruction using the microPET small animal scanner. Phys. Med. Biol. 1998; 43:1001–1013. [PubMed: 9572523]
33. Qi J, Leahy RM. Theoretical study of the contrast recovery and variance of MAP reconstructions from PET data. IEEE Trans. Med. Imaging. 1999; 18:293–305. [PubMed: 10385287]
34. Qi J, Leahy RM. Resolution and noise properties of MAP reconstruction for fully 3D PET. IEEE Trans. Med. Imaging. 2000; 19:493–506. [PubMed: 11021692]
35. Shi HR, Fessler JA. Quadratic regularization design for 2-D CT. IEEE Trans. Med. Imaging. 2009; 28:645–656. [PubMed: 19272993]
36. Stayman JW, Fessler JA. Regularization for uniform spatial resolution properties in penalized-likelihood image reconstruction. IEEE Trans. Med. Imaging. 2000; 19:601–615. [PubMed: 11026463]
37. Swensson RG. Unified measurement of observer performance in detecting and localizing target objects on images. Med. Phys. 1996; 23:1709–1725. [PubMed: 8946368]
38. Yang L, Zhou J, Qi J. Regularization design for breast lesion detection in penalized maximum likelihood image reconstruction. IEEE Intl. Symp. Biomed. Imaging. 2012:626–629.
39. Yao J, Barrett HH. Predicting human performance by a channelized Hotelling model. Proc. SPIE. 1992; 1768:161–168.

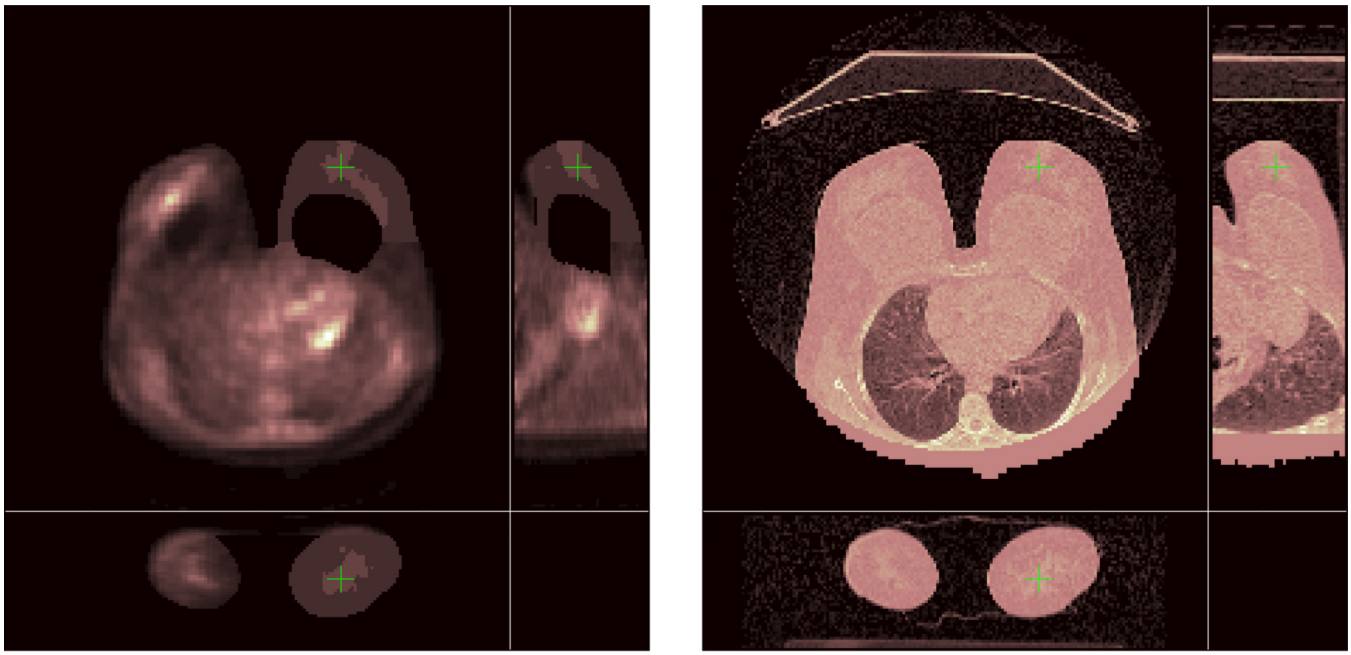

(a) PET phantom (b) CT phantom

Figure 1.
Three orthogonal views of the digital phantom through the green cross.

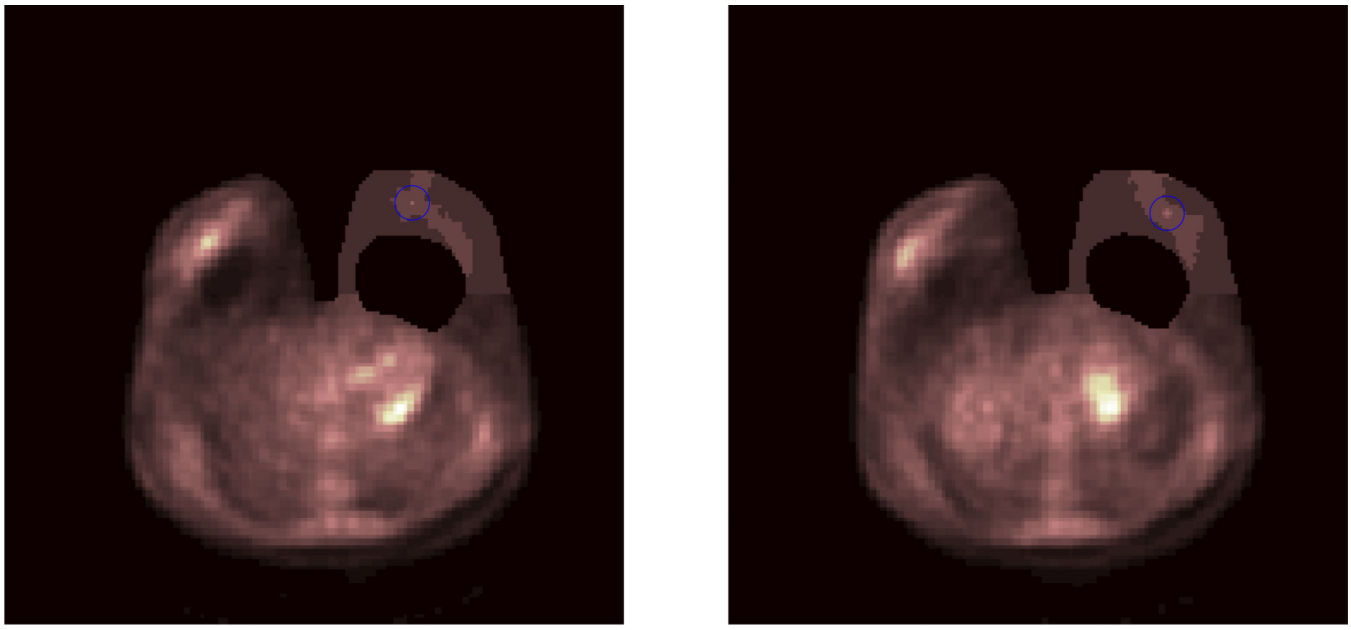

(a) The central slice of the 3 mm lesion (b) The central slice of the 8 mm lesion

Figure 2.
The digital phantom with a simulated lesion in the uniform glandular tissue at the center of the blue circle.

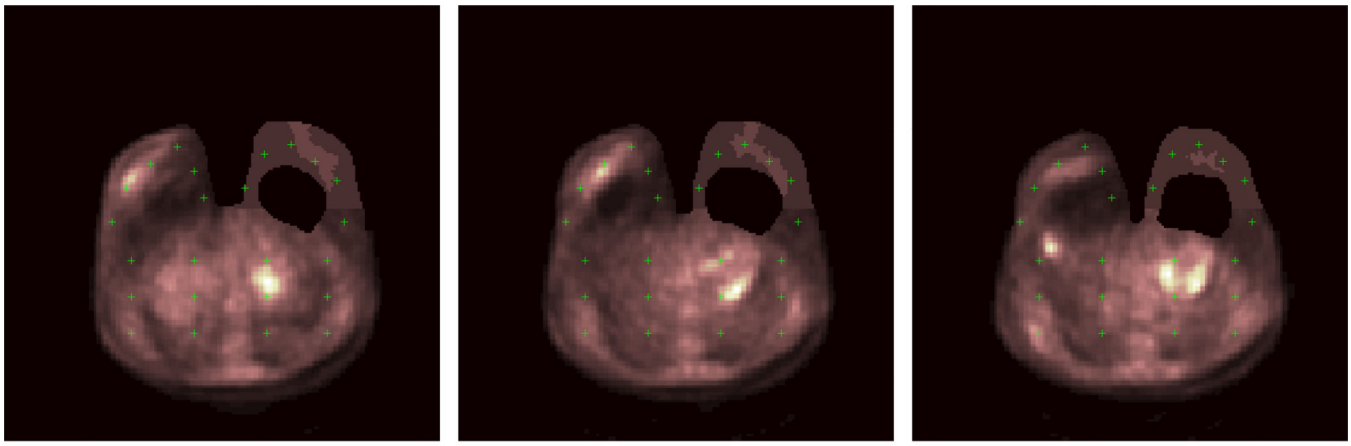

(a) Slice 18 (b) Slice 24 (c) Slice 30

Figure 3.
The 72 selected points (represented by green "+") for calculation the penalty matrix ***R***.

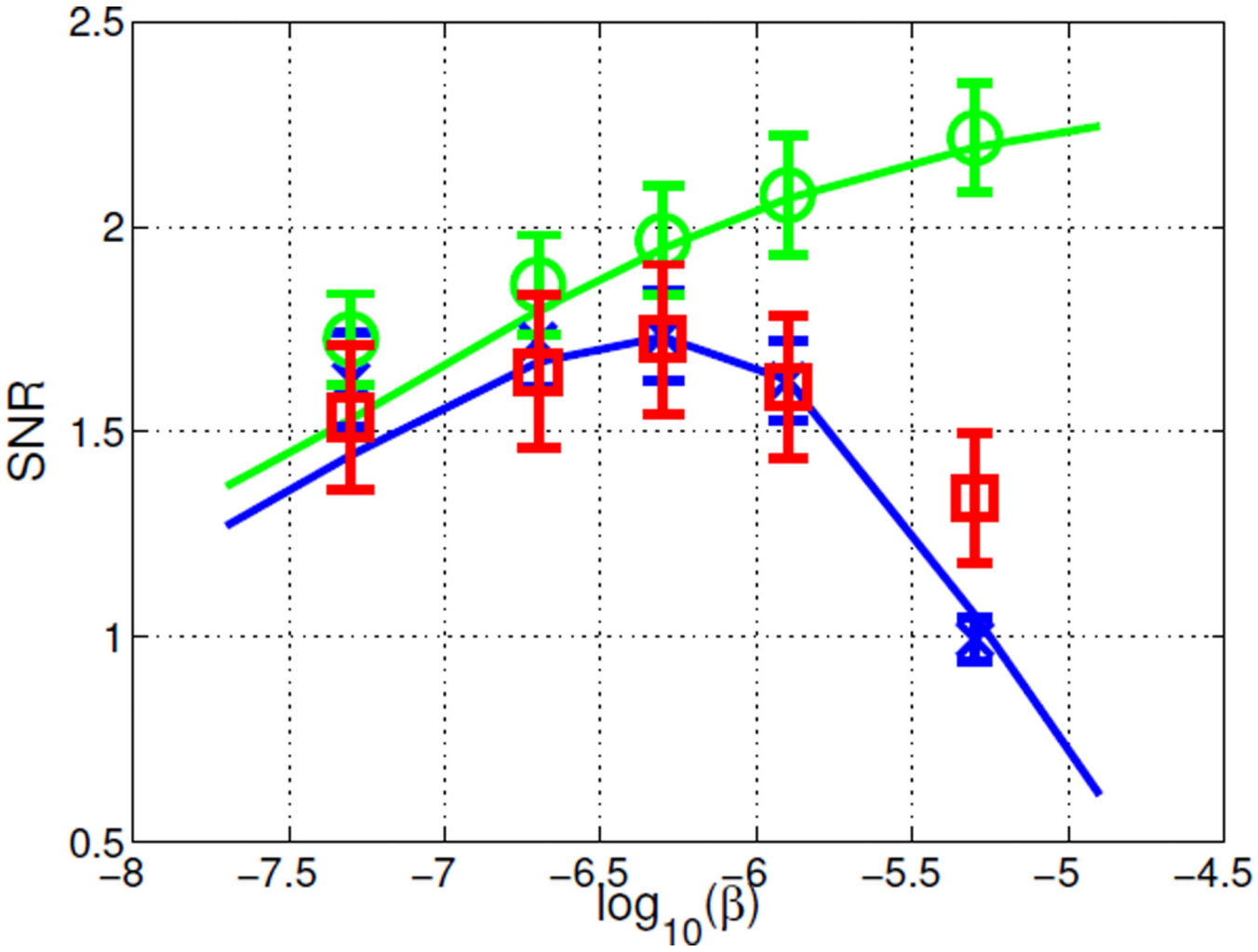

Figure 4.

Comparison of the theoretical predictions with the estimated internal noise model (blue solid line) and those without the internal noise (green solid line), and the human observer performance for one tumor location. The blue crosses and green circles are the respective Monte Carlo SNRs calculated from the 200 noisy images reconstructed with five β values. The human observer results are marked by red squares. The error bars indicate plus and minus one standard deviation.

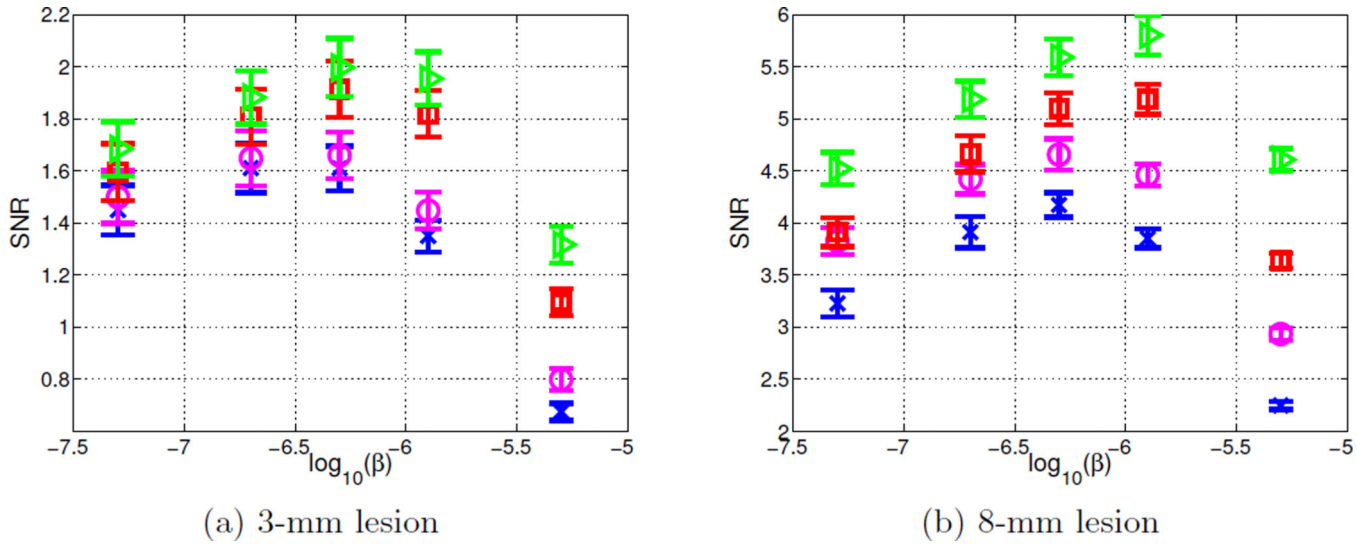

Figure 5.

Comparison of the single slice CHO (blue cross), multislice CHO (pink circle), multiview CHO (red square), and multislice multiview CHO (green triangle) for lesion detection.

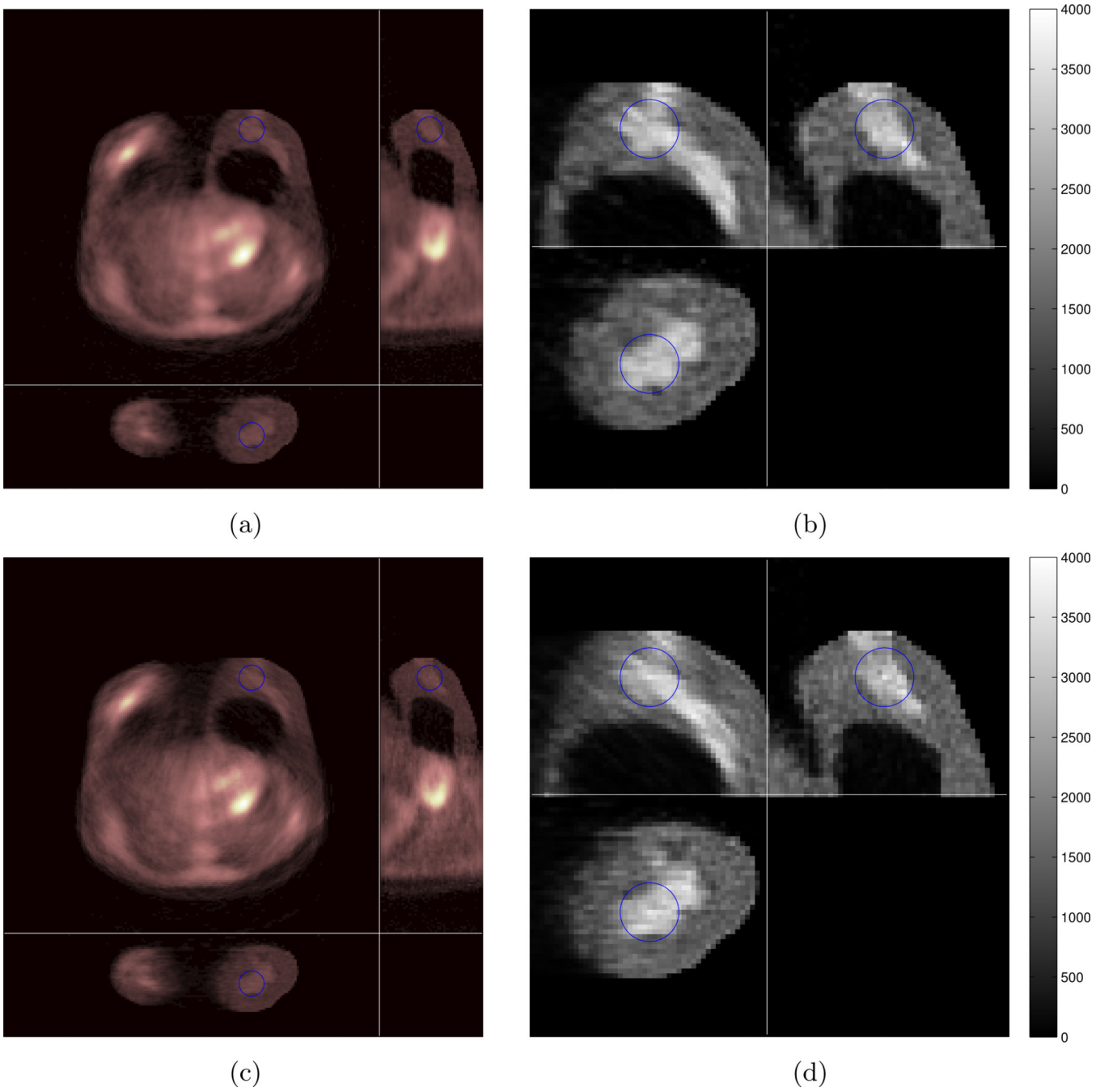

Figure 6.

The sample reconstruction using the first order quadratic penalty function (a) and the proposed penalty function (c), with the respective enlarged breast images shown in (b) and (d). There is a 3 mm lesion at the center of the blue circle.

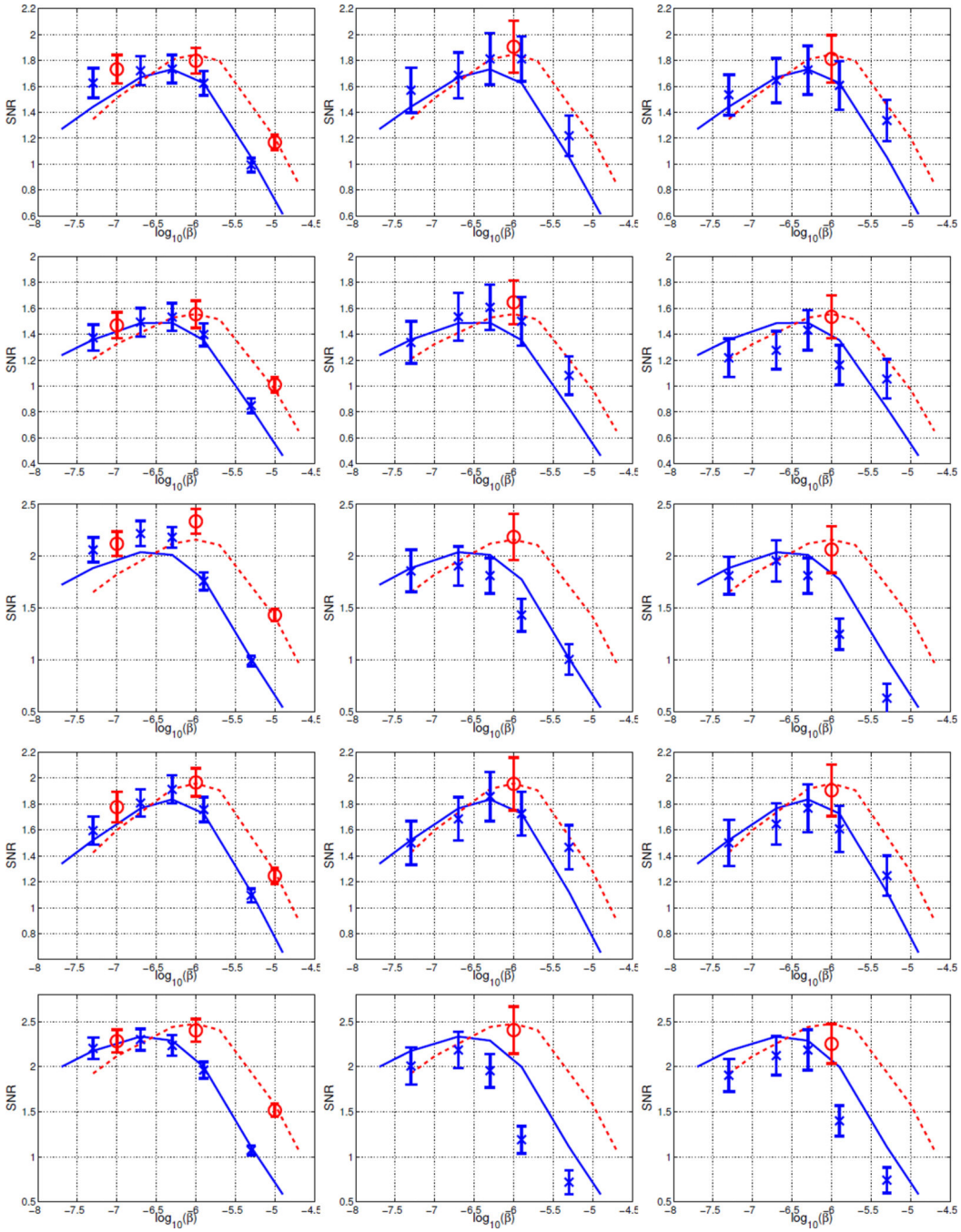

Figure 7.

Comparison of the Monte Carlo results (left column) and human observer study (middle (LY) and right (AF) column) with theoretical predictions using the conventional first-order quadratic penalty (blue solid line) and proposed penalty (red dash line). Each row represents one lesion location. The Monte Carlo and human observer results of the conventional penalty are marked by "' × ' and those of the proposed penalty by "o". The error bars indicate plus and minus one standard deviation.

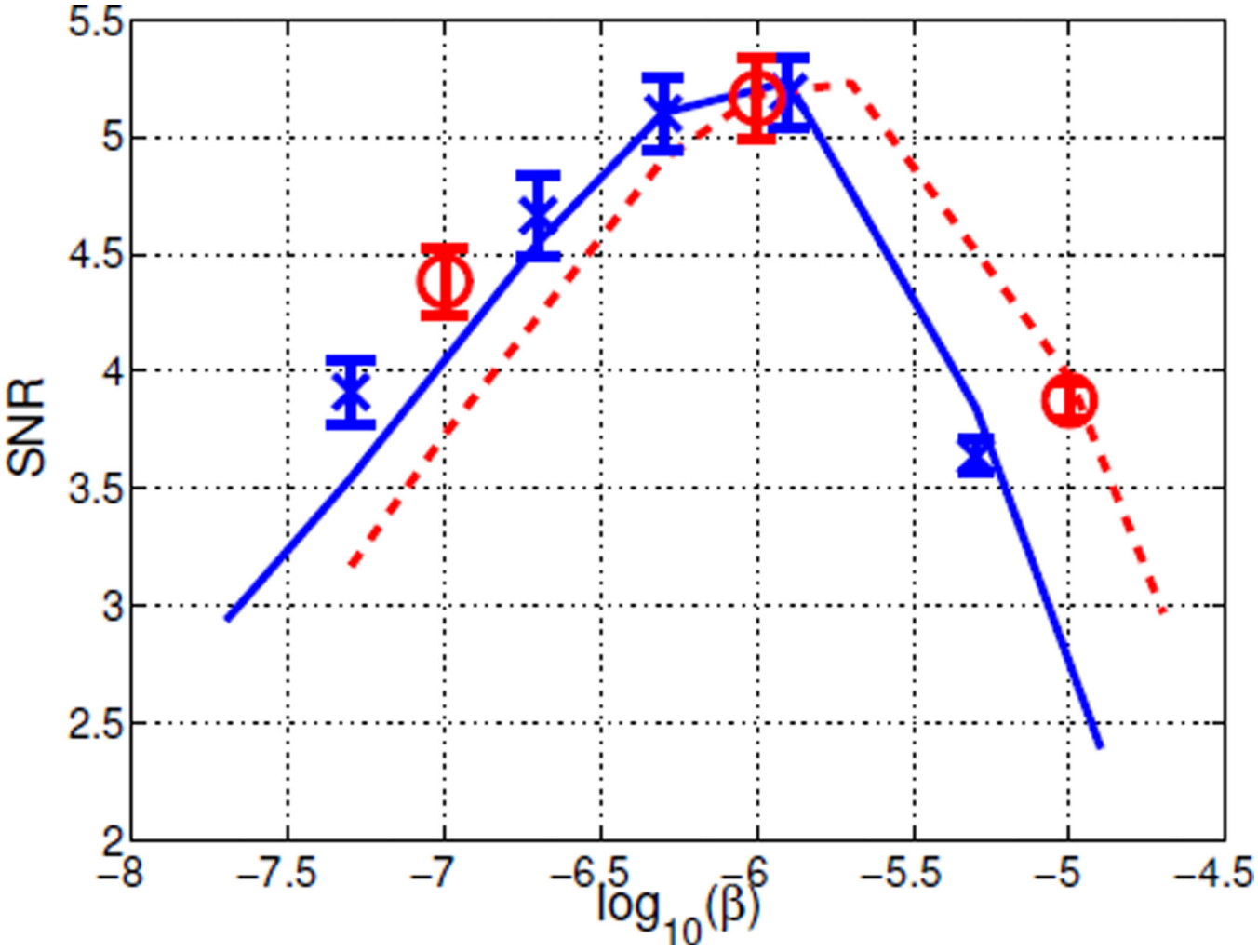

Figure 8.

The detectability of the 8mm lesion in reconstruction with different penalty functions. The red circle denotes the Monte Carlo results of the optimized penalty function, the blue cross denotes the Monte Carlo results of the first order quadratic penalty function.

Table 1

Four categories of the 2AFC experiment outcomes

First order penalty	Proposed penalty	Number of cases
correct	correct	N_1
wrong	wrong	N_2
correct	wrong	N_3
wrong	correct	N_4

Table 2

The McNemar's test results

	LY	**LY**	**AF**	**AF**
	1st order quadratic ($\log_{10}\beta=-6.7$) v.s. proposed penalty	**1st order quadratic ($\log_{10}\beta=-6.3$) v.s. proposed penalty**	**1st order quadratic ($\log_{10}\beta=-6.7$) v.s. proposed penalty**	**1st order quadratic ($\log_{10}\beta=-6.3$) v.s. proposed penalty**
N_1	788	786	775	776
N_2	54	49	61	54
N_3	18	23	21	28
N_4	40	42	43	42
p-value	0.0029	0.0128	0.0043	0.0601